Thermally Mediated Droplet Formation at a Microfluidic T-Junction

Thermally mediated droplet formation at a microfluidic T-junction

Peng-Ching Ho[a] , Yit-Fatt Yap [b] , Nam-Trung Nguyen [a]* , John Chee-Kiong Chai [b]
[a]*School of Mechanical and Aerospace Engineering, Nanyang Technological University, 50 Nanyang Avenue, Singapore, 639798*
[b] *Department of Mechanical Engineering, The Petroleum Institute, P.O. Box 2533, Abu Dhabi, United Arab Emirates.*

*Address correspondence to this author at the School of Mechanical and Aerospace Engineering, Nanyang Technological University, 50 Nanyang Avenue, Singapore, 639798
E-mail: mntnguyen@ntu.edu.sg
Tel: (+65) 67904457
Fax: (+65) 67911859

Abstract: Abstract. This paper reports the investigation on the process of thermally mediated droplet formation at a microfluidic T-junction. The temperature field generated by an integrated heater causes changes in properties of the fluids and affects the droplet formation process. The droplet formation process is formulated in this paper as an incompressible immiscible two-phase flow problem. The motion of the two-phases is strongly coupled by interfacial conditions, which are governed by the three-dimensional Navier-Stokes and the energy equations. The interface or the droplet surface is described by a narrow-band particle level-set method. The numerical solutions of the problem are obtained with finite volume method on a staggered mesh and validated with the experiment data on droplet formation in the dripping regime of a T-junction. The combined effect of the temperature-dependent viscosities and interfacial tension of the fluids results in a larger droplet at elevated temperature. The effectiveness of the penetration of temperature field induced by different heater geometries that resulted in different incremental change in droplet size over a temperature range is discussed.

Keywords: microdroplets, microchannels, level set method, temperature dependency

1. INTRODUCTION

Microfluidics gains popularity in the recent years. Improved mixing [1, 2] and heat transfer [3] in micro scale have been explored. Recently, the field of microfluidics extends from single-phase continuous flow to multi-phase droplet-based flow. With the well controlled droplet-based processes, innovative use of droplets in a wide range of research fields has been proposed. For instance, droplets can act as a container, providing both physical and chemical isolation for its contents. Thus, chemical reaction with only a minute amount of samples can be realized within the droplet. Because of its potential, forming stable droplet of controllable size and frequency is the very first step in droplet-based microfluidics. Different approaches of droplet formation have been proposed and investigated. Droplet formation can be loosely categorized into two groups: passive and active approaches [4]. Passive approaches generate droplets in pure hydrodynamic settings. It generally relies on the geometries of the microchannel, the flow rate ratio and the capillary number to achieve the formation of droplets. Three types of microfluidic geometries [5] used for droplet formation include co-flowing configuration [6], T-junction [7, 8] and flow focusing devices [9-11].

In additional to hydrodynamic means, active approaches add forces induced by external sources. These additional controllable forces modify the underlying hydrodynamics to effectively tune the formation process. External sources include but not limited to thermal [12-14], electric [15, 16] and magnetic fields [17]. A thermal field can be easily generated within a microfluidic device with an integrated heater. The generated heat results in a spatial variation of the temperature-dependent physical properties, such as viscosity, interfacial tension and density. For liquids, viscosities and interfacial tensions are more sensitive to temperature change than densities. The variation in interfacial tension gives rise to thermo-capillary force, i.e. a Marangoni effect. We found in our previous experimental works that larger droplet can be formed with higher temperature induced by a heater and this effect is more profound for microchannels of large aspect ratio, i.e. shallow microchannels [13]. However, much of the physics governing this effect remains unclear. Due to the complex geometry and the strong coupling of the different fields, further understanding has to rely on numerical investigations. Numerical investigation in the physics of passive droplet formations in T-junction [18, 19] and cross-junction [20] have been performed. Computational requirement for simulating a three-dimensional droplet formation process is daunting even for passive droplet formation process. None of the previous works have included thermal effects in the process of droplet formation.

For active droplet formation, numerical investigation is understandably few as this is potentially a multi-physics problem governed by an even larger number of partial differential equations (PDEs). In this paper, the formation of a three-dimensional droplet under an induced thermal field is investigated. The paper starts with a brief description of the problem, its mathematical formulation and solution procedure. Results and discussions are followed by concluding remarks.

2. NUMERICAL MODELLING

Figure 1 shows a typical T-junction with a square cross section. It should be noted that the channel geometry is not just limited to square cross section. Non-square channel can be expected for a T-junction with rectangular geometry. The two inlets are for the continuous phase (oil) and the dispersed phase (water). The continuous phase and the dispersed phase are immiscible. For the convenient of the later implementation of level-set simulation, they are designated as the negative (-ve) fluid and the positive (+ve) fluid. These phases are distinguished in the level set function by their signs. The continuous phase (-ve fluid) flows into the channel at the left inlet with an average inlet velocity of u_{-o}. The

dispersed phase (+ve fluid) enters the other inlet with an average velocity of u_{+o}. Both streams are maintained at an initial temperature of T_o at the inlets. With this configuration, the expected droplet formation process occurs at the T-junction where the two channels join. The shear force and the pressure build-up at the junction break off and forms droplets of the +ve fluid. Subsequently, the formed droplets of +ve fluid flow downstream towards the exit. Fully developed flows are assumed for both inlets. Non-slip condition is enforced at the walls of the channel. Out flow boundary condition is employed at the outlet.

For inducing the temperature field, a heater is attached to the wall at the location shown in Fig. 1. Upon switching on the heater, the temperature of the wall directly adjacent to the heater is raised to T_{set}. Other location of the wall is maintained at a temperature of T_o. At the outlet, zero-gradient is employed. With these boundary conditions, a non-uniform temperature field is established in the channel and changes the local physical properties of both fluids. These thermally induced changes produce additional forces acting on the forming droplet, altering its formation process.

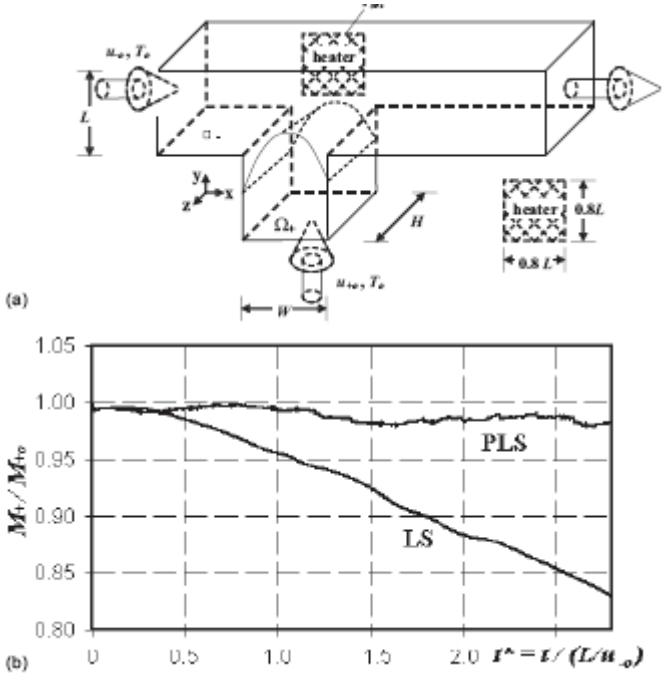

Fig. (1). Droplet formation in a T-junction with thermal forcing: (a) The computational domain (L: width of the channel for continues phase, W: width of the channel for dispersed phase, H: channel height); (b) Mass loses with pure Level Set (LS) Method and Particle Level Set (PLS) method.

Mathematical formulation

The domain of interest consists of the -ve fluid and the +ve fluid. These fluids are separated by the interface Γ. A level-set function [21] is used to represent the interface and can be expressed mathematically as

$$\varphi = \begin{cases} -d, & \vec{x} \in \Omega_- \\ 0, & \vec{x} \in \Gamma \\ +d, & \vec{x} \in \Omega_+ \end{cases} \qquad (1)$$

where d is the shortest normal distance from the interface Γ, $\vec{x}$ is the location in the –ve fluid (Ω_-) as well as in the +ve fluid (Ω_+). Within the present framework, the domain of interest is formulated as a single special fluid. This fluid is special in the sense that its properties at a given time and location are set to the properties of either the -ve or the +ve fluids depending on whichever that occupies that particular location at that particular time. A property α of the special fluid can be conveniently expressed using the level-set function as

$$\alpha(\phi) = (1 - H)\alpha_- + H\alpha_+ \tag{2}$$

where H is a function of the level-set function ϕ:

$$H(\phi) = \begin{cases} 0, & \phi < -\varepsilon \\ \dfrac{\phi + \varepsilon}{2\varepsilon} + \dfrac{1}{2\pi}\sin\left(\dfrac{\pi\phi}{\varepsilon}\right), & |\phi| \le \varepsilon \\ 1, & \phi > +\varepsilon \end{cases} \tag{3}$$

with H smears over a thickness of 2ε, ε is set to be 1.5 times of the mesh size.

The conservation of mass, momentum and energy of the special fluid are formulated mathematically as:

$$\frac{\partial \rho}{\partial t} + \nabla \bullet (\rho \vec{u}) = 0 \tag{4}$$

$$\frac{\partial (\rho \vec{u})}{\partial t} + \nabla \bullet (\rho \vec{u}\vec{u}) = -\nabla p + \nabla \bullet \left[\mu\left(\nabla \vec{u} + \nabla \vec{u}^{\,T}\right)\right] + \vec{f}_F \tag{5}$$

$$\frac{\partial (\rho c_p T)}{\partial t} + \nabla \bullet (\rho c_p \vec{u} T) = \nabla \bullet (k \nabla T) \tag{6}$$

where ρ, μ, c and k are the density, the dynamic viscosity, the specific heat and the thermal conductivity respectively. It can be noted that Eqn. (4) is reduced to $\nabla \bullet (\rho \vec{u}) = 0$ as the fluid in this present study is assumed to be incompressible. In equation (5), the interfacial force given by [22] as

$$\vec{f}_F = -\kappa \sigma \hat{N}_F D(\vec{x} - \vec{x}_F) + \left(\hat{N}_F \times \nabla \sigma\right) \times \hat{N}_F D(\vec{x} - \vec{x}_F) \tag{7}$$

where the Dirac delta function $D(\vec{x} - \vec{x}_F)$, the unit normal to the interface $\hat{N}_F$ and κ are defined respectively as

$$D(\vec{x} - \vec{x}_F) = D(\phi) = \begin{cases} \dfrac{1 + \cos(\pi(\phi)/\varepsilon)}{2\varepsilon} & |(\phi)| < \varepsilon \\ 0 & \text{otherwise} \end{cases}$$

$$\hat{N}_F = \frac{\nabla(\phi)}{|\nabla(\phi)|} \tag{8}$$

$$\kappa = \nabla \cdot \hat{N}_F$$

The first and second terms in (7) account for capillary and thermo-capillary effects respectively. The evolution of the interface Γ is governed by

$$\phi_t + \vec{u} \cdot \nabla \phi = 0 \tag{9}$$

To maintain ϕ as a distance function, ϕ is set to the steady-state solution of the following equation:

$$\frac{\partial \phi'}{\partial \bar{t}} = \overline{sign}(\phi)\left(1 - |\nabla \phi'|\right) \tag{10}$$

where $\bar{t}$ is a pseudo time for second level-set function (employed for redistancing purpose only) ϕ' and $\overline{sign}(\phi)$ is given by

$$\overline{sign}(\phi) = \frac{\phi}{\sqrt{\phi^2 + (\Delta x)^2}} \tag{11}$$

and is subjected to the following initial condition

$$\phi'(\vec{x},0) = \phi(\vec{x}) \tag{12}$$

A particle correction procedure [22, 23] is adopted, to avoid the mass loss problem well known for the level-set method. Massless particles of size in the range of $0.1\Delta x \le r_p \le 0.5\Delta x$, where Δx is the mesh size of the model, associated with each phase are seeded near the interface. These particles are then attracted to the correct side of the interface, i.e. positive particle to the side with $\phi > 0$ and negative particle to the side with $\phi < 0$. The radius of each particle r_p is set to

$$r_p = \begin{cases} r_{\max} & if \quad S_p > r_{\max} \\ S_p & if \quad r_{\min} \le S_p \le r_{\max} \\ r_{\min} & if \quad S_p < r_{\min} \end{cases} \tag{13}$$

where $S_p = \overline{sign}[\phi(\vec{x}_p)]\phi(\vec{x}_p)$

These particles are advected according to

$$\frac{d\vec{x}_p}{dt} = \vec{u}\left(\vec{x}_p\right) \tag{14}$$

where $\vec{x}_p$ is the position of the particle.

The sets of positive and negative particles that happen to be in the opposite side of the interface in the advection process are identified respectively as E^+ and E^-. Two new level-set functions with each associated with the positive and the negative particles, ϕ^+ and ϕ^-, are first initialized as ϕ and then updated according to

$$\phi^+ = \begin{cases} \max(|\phi^+|, |\phi_p|), \phi^+ > 0, \forall p \in E^+ \\ -\max(|\phi^+|, |\phi_p|), \phi^+ < 0, \forall p \in E^+ \end{cases} \tag{15}$$

and

$$\phi^- = \begin{cases} \max(|\phi^-|, |\phi_p|), \phi^- > 0, \forall p \in E^- \\ -\max(|\phi^-|, |\phi_p|), \phi^- < 0, \forall p \in E^- \end{cases} \tag{16}$$

where $\phi_p = sign[\phi(\vec{x}_p)](r_p - |\vec{x} - \vec{x}_p|)$

Particle correction on the level-set function ϕ is performed via

$$\phi = \begin{cases} \phi^+, & \text{if } |\phi^+| \le |\phi^-| \\ \phi^-, & \text{if } |\phi^+| > |\phi^-| \end{cases} \tag{17}$$

In the numerical implementation of the particle correction procedure, $\phi(\vec{x}_p)$ and $\vec{u}(\vec{x}_p)$ are evaluated by trilinear interpolation of their respective values on the underlying nodes. Upon obtaining a converged level-set value ϕ, the sizes of the particles r_p are updated through (13).

Numerical implementation

The conservation equations (4-6) are solved on a staggered grid system by employing a finite volume method with SIMPLER algorithm [24] to resolve the pressure-velocity coupling. The evolution of the level-set function and its redistancing are implemented in a narrow-band procedure [25]. Both are spatially discretized with WENO5 algorithm [26] and advected using TVD-RK2 algorithm [27]. The overall solution procedure is as follow: Given known ϕ, $\vec{u}$, p and T, proceed the solution in time for ϕ^{n+1}, $\vec{u}^{n+1}$, p^{n+1} and T^{n+1}:

Step (1) Set $\vec{u}^{n+1} = \vec{u}^n$

Step (2) Compute ϕ^{n+1} from Eq. (9)

Step (3) Perform redistancing via Eqs. (10-12) and particle correction on ϕ^{n+1} via Eqs. (13-17)

Step (4) Calculate the properties of the special fluid using Eqs. (2, 3).

Step (5) Solve for $\vec{u}^{n+1}$ and p^{n+1} from Eqs. (4, 5) via the SIMPLER algorithm

Step (6) Solve for T^{n+1} from Eq. (5).

Step (7) Iterate step (2) through (6) and check if solution converges

Step (8) If solution converges, proceed to the next time step by starting from step (1). Otherwise, terminate the procedure.

3. RESULTS AND DISCUSSIONS

We first validate the numerical procedure with experimental and numerical data of the cross-flow configuration reported by Wu et al. [20]. The optimised PLS settings are examined using a generic channel geometry but based on a specific set of hydrodynamic condition of our experimental results previously reported in [13]. The effect of thermal penetration based on the heater arrangement was investigated and compared to experimental results.

Validation

As mentioned above, a first-level validation on the present procedure was performed for droplet formation with flow-focusing configuration. Figure 2 compares our prediction with both experimental and numerical results with Latice-Boltzmann methods reported in [20]. The qualitative comparison has shown that the result from our present procedure is in good agreement with the experiment and numerical solution. This preliminary validation exercise shall also serve as a starting point to demonstrate the applicability of the present numerical approach for droplet formation in different microfluidic geometries such as cross-flow configuration or T-channel which was employed in the later part of this investigation.

Following up the preliminary validation result, the next level of validation was carried out to determine the optimized settings of our numerical procedure in specific to the set of hydrodynamic condition upon which the experimental study was conducted. The evaluation and selection of the optimized settings of the present procedure will now be discussed.

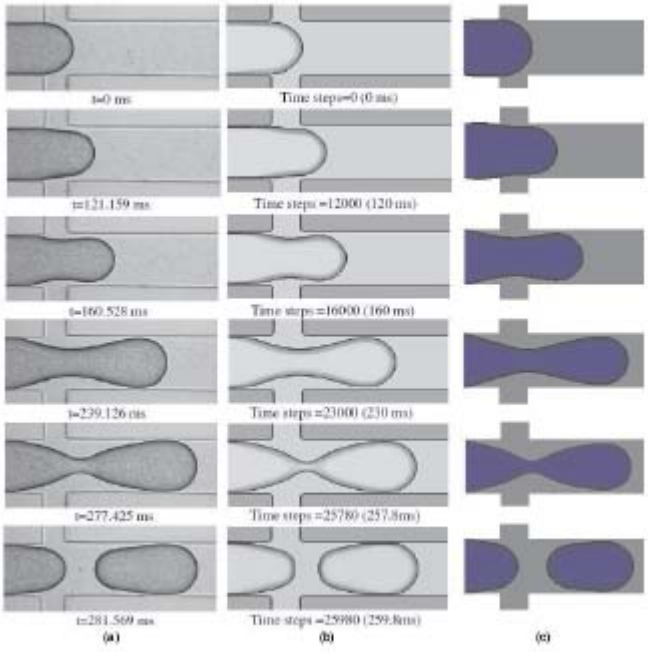

Fig. (2). Droplet formation in a cross-junction: (a) experimental [20]; (b) numerical [20]; (c) present algorithm.

The requirement on computational resources, both computational power and computer memory, of a three-dimensional model is enormous. Therefore, the computational demand of the modeled domain is made as minimal as possible but with an acceptable level of accuracy and stability of the numerical solution. In the case of a VOF-based numerical model [28], it was reported that at a flow condition of 13m/s to 26m/s for a -ve fluid (air) and 0.09m/s to 0.18m/s for a +ve fluid (water), only minor difference can be seen for cases ranging from 78 x 10^3 and 320 x 10^3 of computational nodes for the given domain of 5mm x 500μm x 45μm. A mesh of 120 x 10^3 nodes was ultimately selected for the use in the numerical simulation in consideration of the computational cost and the insignificant difference in the accuracy of the numerical solution. Generally speaking, for any hydrodynamic numerical model, channel size and flow condition are factors affecting the optimal mesh to be used in the simulation in order to achieve good accuracy and with reasonable computational expense. In other words, the optimal mesh density and consequently the number of computational nodes are highly dependent on the channel size and flow condition.

As explained earlier in section 2.1, a particle correction procedure [23] was adopted to address the well known mass loss problem of a level-set method for our present study. Figure 1(b) shows the mass loss of water droplet over time for the case of a generic T-junction geometry resulting from our present procedure. M_{+o} and M_{+} are the correct and current mass of the droplet. The ratio $M_{+}/M_{+o} = 1$ corresponds to the case of perfect mass conservation. Mass loss increases over time for a pure level-set method. For the case, a mass loss of around 17% is incurred with pure level-set method. The trend shown in Fig. 1(b) indicates that mass loss increases over time. However, activating the particle correction procedure allows keeping the mass loss well under 3%. This fact affirmed the proper functionality of our Particle Level Set (PLS) numerical procedure in addressing mass loss phenomena.

The particle level set method involves the setting of particle related parameters such as particle re-initialisation scheme, particle density and seeding interval. Therefore, besides the number of nodes, several other settings of the Particle Level Set (PLS) method also need to be considered in order to achieve reasonably accurate numerical results [29].

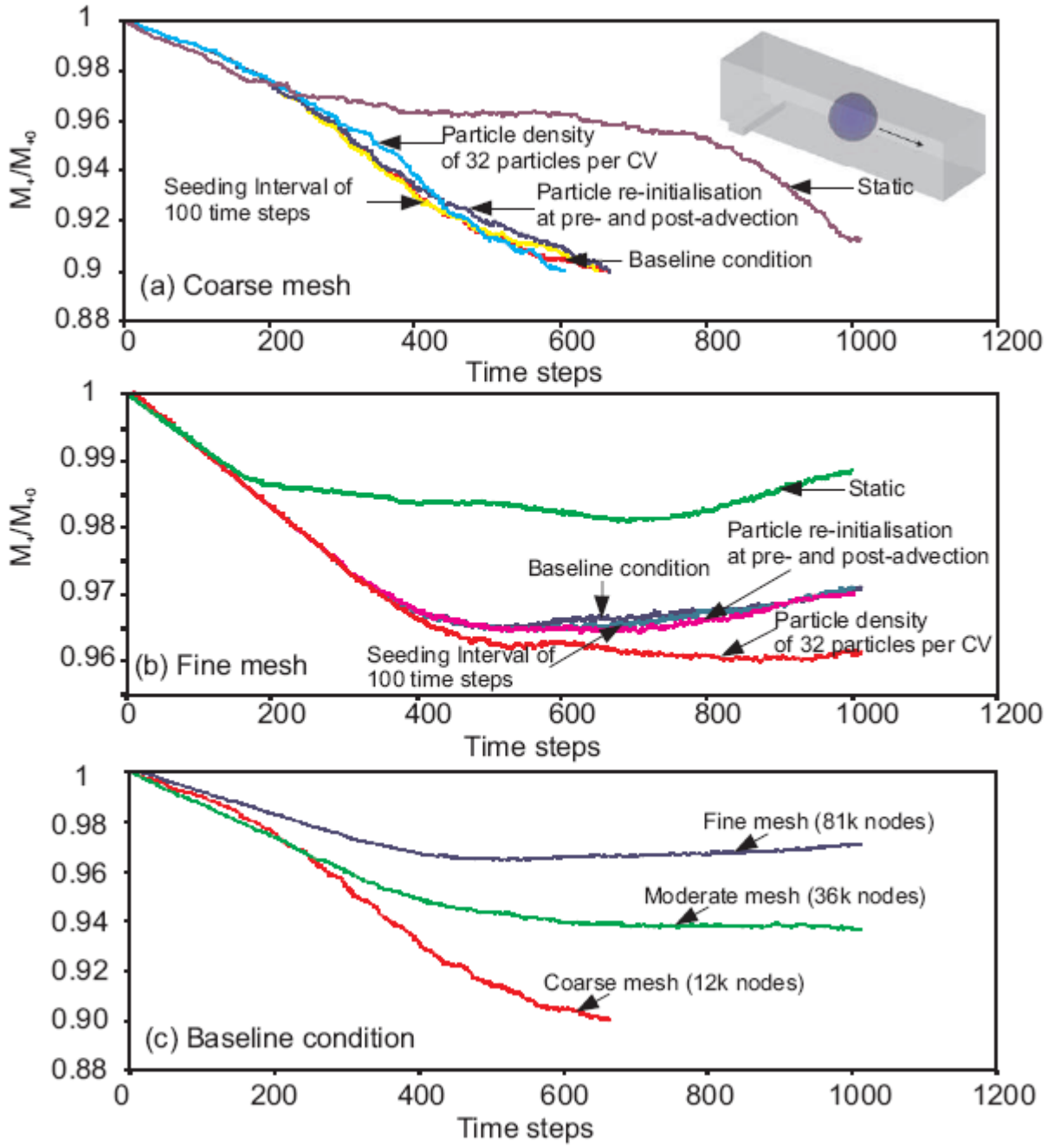

Fig. (3). Mass losses of various particle level set conditions : (a) Coarse mesh with 12 x 10^3 nodes; (b) Fine mesh with 81 x 10^3 nodes; (c) Different mesh density at baseline conditions.

The settings of the particle related parameters are validated prior to the start of the actual numerical investigation. This is carried out by simulating a spherical water droplet flowing in a square channel of 50μm x 50μm x 250μm with the same hydrodynamic flow condition as in the experimental study [Inserts in Figure 3(a)]. The hydrodynamic flow condition is governed by dimensionless numbers which will be discussed in the next section. As mass conservation is a

critical index to the success of a PLS numerical model, the validation is based on the mass loss performance. Two different mesh setups are evaluated - coarse and fine mesh of 12 x 10^3 and 81 x 10^3 nodes, respectively. For each of the mesh setup, different settings are tested: 1) particle re-initialisation at post advection of the interface versus at both pre- and post-advection 2) particle density of 64 particles per control volume (CV) versus 32 particles and 3) seeding interval of 200 versus 100 time steps. The baseline settings are re-initialisation at post-advection, 64 particles per CV and 200 time step seeding interval. Figures 3(b) and 3(c) show the mass loss of the droplet over time for coarse and fine mesh respectively at different settings.

In the case of coarse mesh as shown in Fig. 3(a), the mass of droplet for the baseline setting is eroding over time and reaches 90% of the exact mass after 700 time steps. As compared to the baseline setting, similar trend on the degradation of mass loss for the other PLS settings can also be observed (i.e. pre- and post advection particle re-initialization scheme, 100 time steps seeding interval and 32 per CV particle density). The worst among them is the seeding density of 32 particles per CV. If the flow condition is isolated, as in the case of the static flow, the mass loss phenomena is less drastic. However, a significant mass loss still happens eventually after 800 time steps. This result illustrates the impact of flow condition and would mean that the optimal grid for any domain is dependent on the flow condition.

For the case of the fine mesh [Fig. 3(b)], tremendous improvement can be seen in the mass loss performance as compared to the coarse mesh. The fine mesh has also reduced the sensitivity of the various PLS settings. Similar to the case of coarse mesh, the mass loss performance is most sensitive to particle density although the impact is not considered to pose any major concern as it has shown to reach stability. Based on the results from the fine mesh, the baseline condition is validated to be acceptable for the present study. Under a no flow condition, the static case shows a superior performance in term of mass loss. This result has further confirmed the effect of flow condition.

Considering the computational expense, a moderate mesh of 36 x 10^3 nodes is selected. The selection is based on the mass loss performance index at the baseline condition. In Figure 3(c), the moderate mesh has shown to be acceptable for the present study as compared to the fine and coarse mesh discussed earlier. The validation exercise concludes that there is no absolute one-size-fits-all mesh setup. The optimal setting is specific to the hydrodynamic flow condition employed in the numerical experiment.

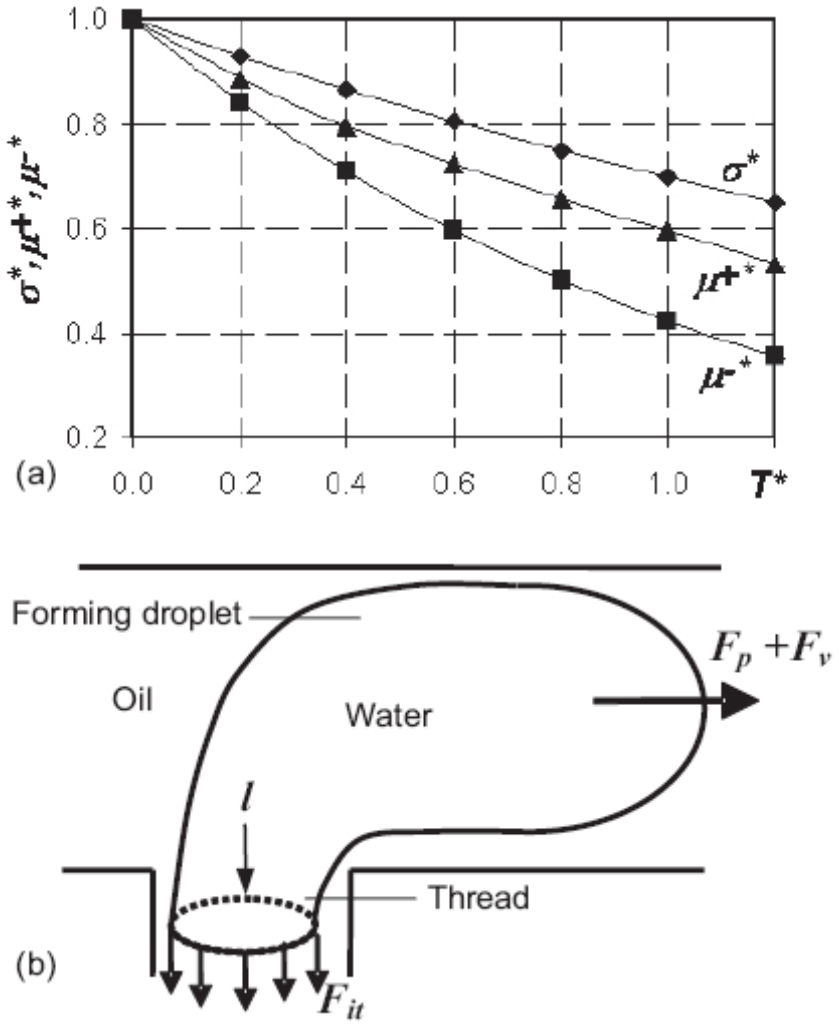

Fig. (4). Numerical model: (a) Temperature dependency of thermo-physical properties of the fluids; (b) Forces acting on the forming droplet at a T-junction.

Numerical solution

The formation of water droplet in mineral oil is considered in our numerical investigation. The -ve fluid and the +ve fluid represent mineral oil and water, respectively. The temperature dependent properties of these fluids normalized by their corresponding values at $T_o = 25^oC$ were fitted as polynomial functions from the experimental data reported in [14] as

$$\mu_-^* = \frac{\mu_-}{\mu_{-o}} = 4.57 \times 10^{-2} T^{*2} - 3.46 \times 10^{-1} T^* + 1.0 \qquad (18)$$

$$\mu_+^* = \frac{\mu_+}{\mu_{+o}} = -1.41 \times 10^{-1} T^{*3} + 3.75 \times 10^{-1} T^{*2} - 6.38 \times 10^{-1} T^* + 1.0 \qquad (19)$$

$$\sigma^* = \frac{\sigma}{\sigma_o} = -4.70 \times 10^{-2} T^{*3} + 3.07 \times 10^{-1} T^{*2} - 8.37 \times 10^{-1} T^* + 1.0 \qquad (20)$$

where $T^* = (T - T_o) /T_o$ is the dimensionless temperature, $\sigma_o = 3.65\times10^{-3}$ N/m, $\mu_{-o} = 1.20\times10^{-2}$ Pa.s and $\mu_{+o} = 1.00\times10^{-3}$ Pa.s are the interfacial tension, viscosity of oil and viscosity of water at the reference temperature of $T_o = 25^oC$. Figure 4(a) shows the relationships between the above properties and the temperature. In general, these properties vary almost linearly over the small range of temperature change considered in our problem.

Since the densities of both fluids are considered as temperature independent in the problem and buoyancy can be neglected in microscale, the densities of both fluids are set to 1000 kg/m^3 [18-20]. The main channel is filled with continuously flowing mineral oil as the forming droplet develops. A layer of oil is always present between the droplet and the channel wall. Therefore, the droplet will not come into direct contact with the wall and thus, the absence of moving contact line. Base on this assumption, contact angle will not be taken into account in our problem.

To generalize the numerical results, instead of presenting them with dimensions, it is more convenient to display them in a dimensionless form. With geometrical similarity maintained, the present problem is governed by a total of 7 dimensionless numbers: the Reynolds number $Re_o = \rho\ u_{-o}L/\mu_{-o}$, the capillary number $Ca = u_{-o}\ \mu_{-o}/\sigma_{-o}$, the Prandlt number $Pr_o = \mu_{-o}/a_{-o}$, the dimensionless heater temperature $T^*_{set} = (T_{set} - T_o)/T_o$, the viscosity ratio $\mu^* = \mu_{+o} /\mu_{-o}$, the flow rate ratio $u^* = u_{+o} /u_{-o}$ and the ratio of thermal diffusivities $a^* = a_+ /a_-$. L is the base length which is 50μm for this case. As the purpose of the present investigation is to study the effect of a thermally mediated droplet formation process, all the above dimensionless parameters are fixed except the dimensionless heater temperature. The conditions of the investigated problem are $Re_o = 4.63\times10^{-4}$, $Ca_o = 3.65\times10^{-2}$, $Pr_o = 1.02\times10^3$, $\mu^* = 8.33\times10^{-3}$, $u^* = 1.0$ and $a^* = 1.21$. Different dimensionless heater temperatures, T^*_{set}, of values 0.0, 0.04, 0.2, 0.36, 0.44 and 0.56 were investigated. The time t and the volume V_d of the formed droplet size are non-dimensionalized as $t^* = t/ (L/u_{-o})$ and $V^* = V_d /L^3$ respectively. As shown in the validation exercise, a moderate mesh was selected for the case study. For the same hydrodynamic flow conditions, this corresponds to 15 control volumes spanning across the channel width L which gives a total of 78 x 10^3 nodes for the computational domain. A time step size of 5 x 10^{-5} sec was used.

Before proceeding further, it is beneficial to briefly discuss various forces acting on a forming droplet. Figure 4(b) shows the pressure force F_p generated by the streamwise pressure difference across the forming droplet, the viscous force F_v due the viscous stress acting on the interface of the forming droplet and the interfacial tension force F_{it}. Pressure force F_p and viscous force F_v push the forming droplet downstream. Interfacial tension force F_{it} increases with larger interfacial area of the forming droplet. For Newtonian fluids, this force is proportional to the viscosity and velocity gradient. Interfacial tension force F_{it} keeps the forming droplet from detachment. This force is proportional to the interfacial tension σ and the circumference of the water thread l.

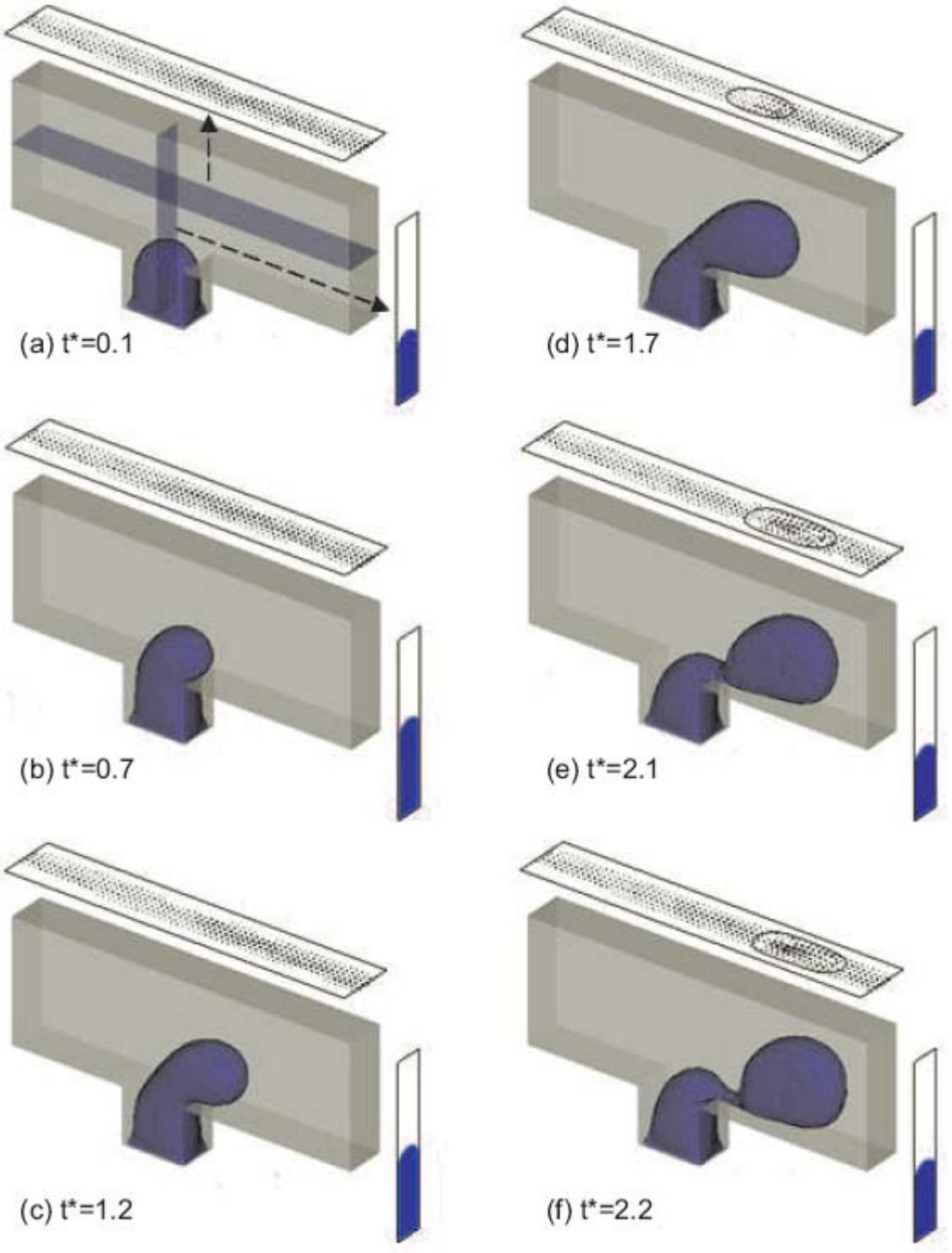

Fig. (5). Droplet formation without induced temperature field (T^*_{set} = 0.0) with sections for the planes y/L = 2.0 and x/L = 2.5.

Droplet formation without temperature field

Figure 5 shows the droplet formation process for the case without the induced temperature field (T^*_{set} = 0.0). Two additional sections of the channel at y/L = 2.0 and x/L = 2.5 are included. The section at x/L = 2.5 indicates the profile

of the forming droplet across the channel. Figure 6 shows another section of the channel at plane z/L = 0.5. These sectional views of the channel are presented for the ease of explanation.

As the water enters into the channel and intersects with the continuous flow of oil, an interface layer is formed between the two phases and the water droplet begins to form. This forming droplet is withheld from detaching by the interfacial tension force F_{it}. As the drop grows, it progressively blocks the cross section of the main channel and obstructs the flow of the continuous phase (oil) causing pressure build-up upstream of the forming droplet (Fig. 5) and increasing the pressure force F_p. At the same time, the flowing oil exerts a viscous force F_v in the form of surface stress on the forming droplet. Both the pressure force F_p and viscous force F_v push the forming droplet downstream thinning the water thread. This process continues to stretch the water thread and making it thinner as shown in Figs. 5(d-e). A thin water thread has a smaller circumference l and therefore weakens F_{it} which withholds the forming droplet from detachment. Besides, interfacial tension effect creates a region of high pressure within the thread where it is the thinnest and has the largest curvature. The water in the thread is then pushed both upstream and downstream away from this region of high pressure within the thread. This further makes the water thread even thinner until the interfacial tension force F_{it} is no longer sufficiently strong to withhold the forming droplet. The water thread breaks and results in the formation of a water droplet. As shown in Figure 6, the various stages of droplet formation process of the numerical procedure agree qualitatively well with the images extracted from the experiment [13].

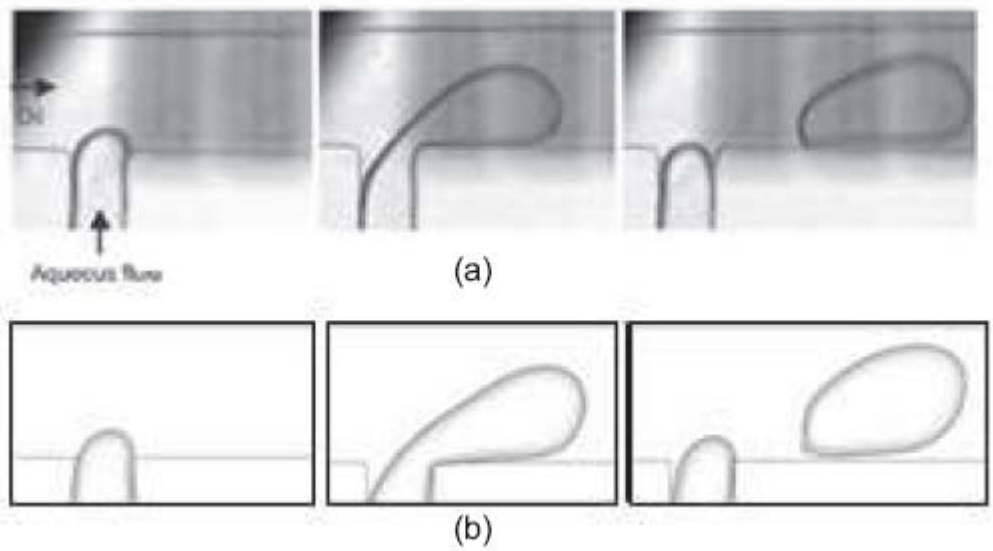

Fig. (6). Droplet formation process (z/L=0.5): (a) Experiment [13]; (b) Present numerical procedure.

Thermally mediated droplet formation

The present study found that heating schemes has an important effect on the formation process. Single-sided and double-sided heating schemes were modeled and evaluated to emulate the same effect of temperature field distribution within the channel as that of the experiment and ultimately to achieve the same order of increase in droplet size at elevated temperature. Unfortunately, no experimental data on temperature distribution within the channel was reported in [13] for a more precise correlation.

The numerical model follows the reported experiment, where the heater was attached to one side of the channel and was located at the intersection of the inlets. This heating scheme is referred to as single-sided. Figure 7 shows the droplet

formation process with a heater temperature of T^*_{set} = 1.0. The temperature field at the plane y/L = 2.0 is also shown. The sectional views of the front and top of the channel are presented as the inserts of Fig. 8.

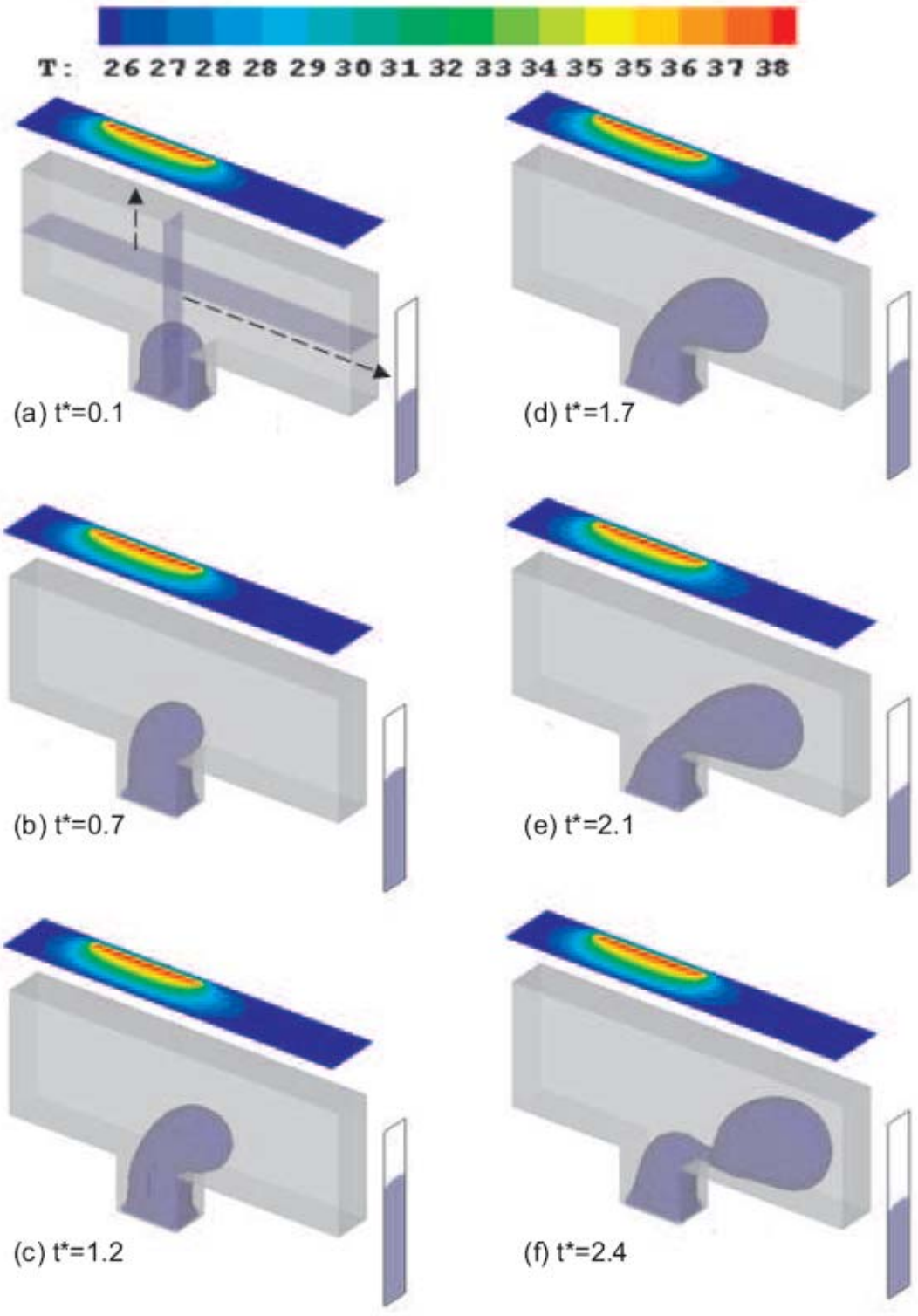

Fig. (7). Droplet formation of single-side heating scheme at T^*_{set} = 1.0 with sections for the planes y/L = 2.0 and x/L = 2.5.

Because the heater is attached to one side of the channel, the temperature field is asymmetrical. The temperature field generated is rather localized with a higher temperature near the inner wall where the heater is located. From the numerical results, the temperature field does not appear to penetrate very far into the flowing fluids. However the layer

of oil between the forming droplet and the hot wall is thin, and much of the heat generated can be transferred into the forming droplet. As water has a much larger thermal conductivity than oil, the temperature field penetrates much further into the forming droplet. This is a desirable effect because the induced temperature field helps to cause a larger change in properties of a larger portion of the oil-water interface. Therefore, the small patch of localized heating is sufficient to cause visible change in droplet size.The size of the droplet formed at different heater temperatures. Without the induced temperature field, a droplet of size V^* = 1.06 is formed. The size increases monotonically to V^* = 1.28 at a heater temperature of T^*_{set} = 0.56 which corresponds to a temperature of T = 39ºC. This means an increase of 20% in the droplet size.

To understand such an increase in the formed droplet size, attention is paid to the change in fluid properties at elevated temperature as shown in Fig. 4(a). An increase in the overall temperature of both oil and water results in smaller interfacial tension and viscosities. The sole effect of a smaller interfacial tension tends to suggest that a smaller interfacial force F_{it} withholding the forming droplet. Therefore, the forming droplet can easily break off, leading to smaller droplet. This is however not the case as the decrease in viscosities is more significant [Fig. 4(a)] and therefore plays the dominant role in this process. A smaller viscosity effectively reduces the viscous force F_v. With a reduction in F_v, the detachment of the forming droplet is delayed. For the case without induced temperature field, the detachment of the forming droplet occurs at t^* = 2.2. With the induced temperature field, detachment of the forming droplet is delayed and occurs at around t^* = 2.4. During the additional time Δt^* = 0.2, more water can flow into the forming droplet through the thread leading to a larger droplet size.

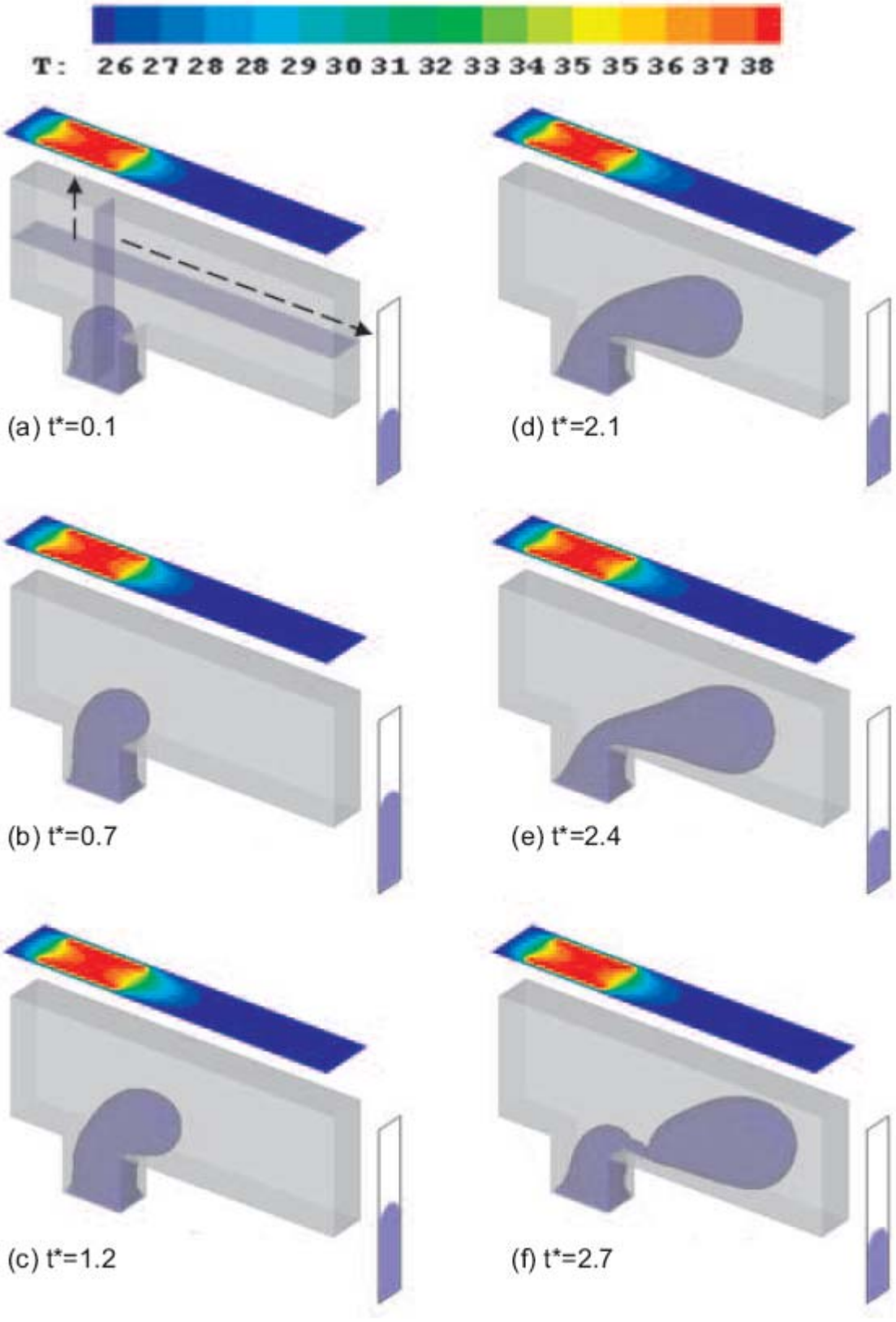

Fig. (8). Droplet formation of single-side heating scheme at T^*_{set} = 1.0 with sections for the planes y/L = 2.0 and x/L = 2.5.

Even though the single-sided heater has demonstrated its effect in changing the fluid properties, the limited penetration depth of heat flux from the heat source into the critical droplet forming area can only have influence on a limited volume of fluid which is exposed to the temperature. In order to further increase the heating effectiveness, the double-

sided heating scheme is simulated. As shown in Figure 8, heaters are placed on both sides of the channels and improve the penetration of the heat flux inside the channel. A more uniform heat distribution can be observed at the critical droplet formation area.

Figure 8 shows the isometric and sectional views of the droplet formation process of the double-sided scheme at T^*_{set} = 1.0. It should be noted that the model has a longer exit channel than that of the single-sided case. The longer channel accommodates the development of a larger forming droplet as expected from the double-sided heating scheme. The solution of our present numerical procedure shall be independent of the change as the critical aspect ratios of the channel are maintained as before.

Figure 9 compares the results of numerical simulation and experiments. With the improved temperature distribution within the channel, the change in the fluid properties is more prevailing for the double-sided heating scheme. As compared with single-sided heating scheme, the increase in droplet size of the double-sided heating scheme can approach that of the experiment. There could be a few reasons for the discrepancies between experiments and the numerical models. On the one hand, the thermal boundary conditions and thus the temperature distribution can not be determined precisely in the experiment. On the other hand, the numerical model presents a more 'localised' heating effect as compared to the actual experiment. In order to correlate their effect with experiment, the actual penetration and spreading of the temperature will have to be better represented in the numerical model.

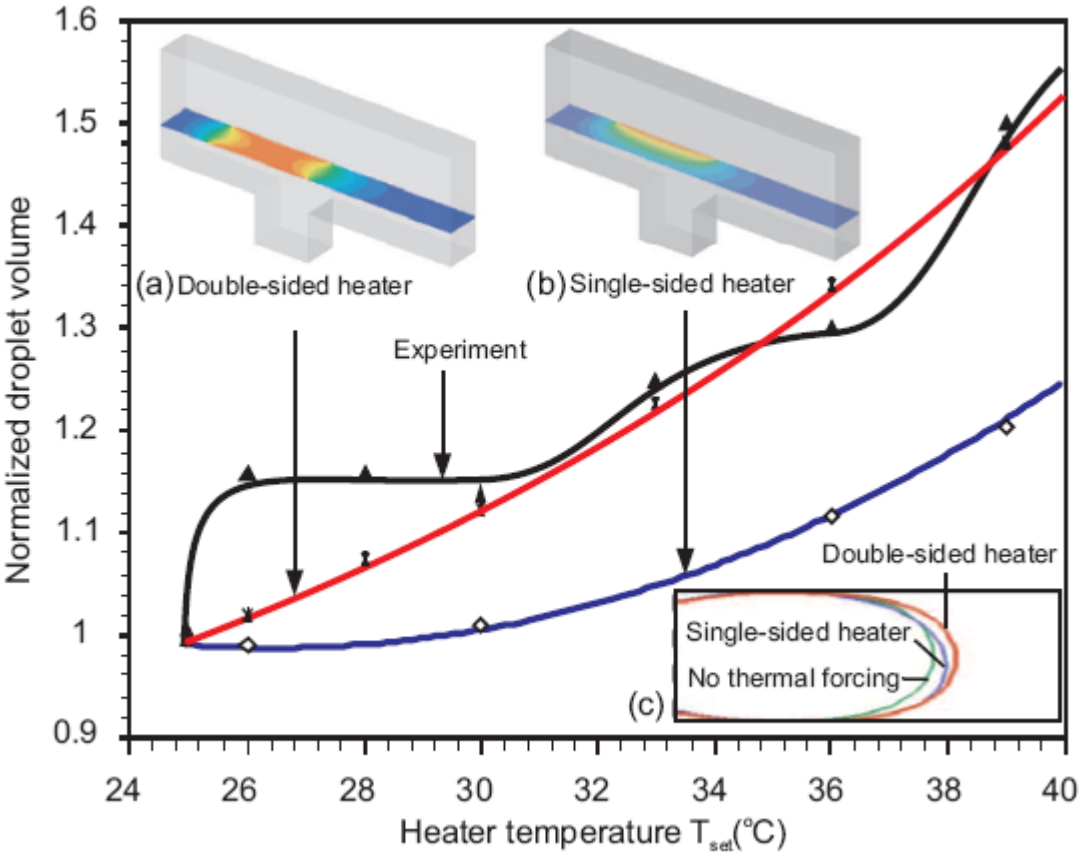

Fig. (9). Droplet size of optimized simulation results and experiment [13]. The volume is normalized by the initial volume without heating at 25ºC. Inserts: (a) temperature field of the double-sided heating scheme; (b) temperature field of the single-sided heating scheme; (c) comparison of droplet shape during its formation.

In thermally induced droplet droplet formation, the phenomenon of thermo-capillary effect is present. Figure 9(c) shows the cross sectional view of the droplet at the plane x/H = 2.5 (single-sided case) and x/H = 1.5 (double-sided case). In the single-sided case, the droplet is observed to be inclining towards the right side of the channel where the heater is positioned. The asymmetrical temperature field generated by single-sided heating scheme created the thermo-capillary effect which draws the forming droplet toward the region of the higher temperature. For the double-sided case, this effect cannot be clearly observed from the cross-sectional droplet profile even though the thermo-capillary effect is present if not stronger. Due to the symmetrical temperature field distribution, the forming droplet in the double-sided heating scheme develops symmetrically across the channel. This profile is similar to the case without thermal forcing.

5. CONCLUSIONS

This paper reports the three-dimensional numerical simulation of the droplet formation process in a microfluidic T-junction under an induced temperature field. Formation of water droplet in oil in the dripping regime was performed as a case study and compared with experiment data. The validation exercise showed that the optimal mesh density is dependent on the flow condition. In the present model, the roles of lower viscosities and interfacial tension of the fluids were explored in the droplet formation process. Thermal forcing was provided by a heat source. Different heating schemes - single and double-sided - are modeled to achieve a correlation to experimental data. Thermo-capillary effect drives the forming droplet towards the region of higher temperature allowing the generated heat to penetrate further into the forming droplet. This phenomenon increases the effectiveness of the applied temperature field. The effect is more noticeable for the single-sided case which has an asymmetrical temperature field. However, this does not undermine the absence of the thermo-capillary effect on the double-sided case. Double-sided heating scheme provides a more uniform heat distribution and thus better heat penetration within the channel. As a result, a larger droplet size can be seen at elevated temperature. In terms of the increase in droplet size over a temperature range from 25ºC to 39ºC, the present numerical solution with the optimized heater geometry showed the same trend as the experimental data. However, only the double-sided heating scheme can achieve the magnitude of change in droplet size as observed in the experiments. The numerical procedure presented in this paper can also be extended to other channel geometries.

REFERENCES

[1] Grigoriev, R.O., Chaotic mixing in thermocapillary-driven microdroplets. *Phys. Fluids*, **2005**. *17*(3): p. 033601-1-033601-8.

[2] Wu, Z. and N.T. Nguyen, Rapid mixing using two-phase hydraulic focusing in microchannels. *Biomed. Microdevices*, **2005**. *7*(1): p. 13-20.

[3] Nguyen, N.T., D. Bochnia, R. Kiehnscherf, and W. Dotzel, Investigation of forced convection in microfluid systems. *Sens. Actuators, A*, **1996**. *55*(1): p. 49-55.

[4] Nguyen, N.T. and X. Huang, Thermocapillary effect of a liquid plug in transient temperature fields. *Jpn. J. Appl. Phys., Part 1: Regular Papers and Short Notes and Review Papers*, **2005**. *44*(2): p. 1139-1142.

[5] Christopher, G.F. and S.L. Anna, Microfluidic methods for generating continuous droplet streams. *J. Phys. D: Appl. Phys.*, **2007**. *40*(19): p. R319-R336.

[6] Cramer, C., P. Fischer, and E.J. Windhab, Drop formation in a co-flowing ambient fluid. *Chem. Eng. Sci.*, **2004**. *59*(15): p. 3045-3058.

[7] Thorsen, T., R.W. Roberts, F.H. Arnold, and S.R. Quake, Dynamic pattern formation in a vesicle-generating microfluidic device. *Phys. Rev. Lett.*, **2001**. *86*(18): p. 4163-4166.

[8] Garstecki, P., M.J. Fuerstman, H.A. Stone, and G.M. Whitesides, Formation of droplets and bubbles in a microfluidic T-junction - Scaling and mechanism of break-up. *Lab Chip,* **2006**. *6*(3): p. 437-446.
[9] Xu, Q. and M. Nakajima, The generation of highly monodisperse droplets through the breakup of hydrodynamically focused microthread in a microfluidic device. *Appl. Phys. Lett.*, **2004**. *85*(17): p. 3726-3728.
[10] Tan, Y.C., V. Cristini, and A.P. Lee, Monodispersed microfluidic droplet generation by shear focusing microfluidic device. *Sens. Actuators, B*, **2006**. *114*(1): p. 350-356.
[11] Anna, S.L., N. Bontoux, and H.A. Stone, Formation of dispersions using "flow focusing" in microchannels. *Appl. Phys. Lett.*, **2003**. *82*(3): p. 364-366.
[12] Tan, S.H., et al., Thermally controlled droplet formation in flow focusing geometry: Formation regimes and effect of nanoparticle suspension. *J. Phys. D: Appl. Phys.*, **2008**. *41*(16).
[13] Murshed, S.M.S., et al., Microdroplet formation of water and nanofluids in heat-induced microfluidic T-junction. *Microfluid. Nanofluid.*, **2009**. *6*(2): p. 253-259.
[14] Nguyen, N.T., et al., Thermally mediated droplet formation in microchannels. *Appl.Phys. Lett.*, **2007**. *91*(8).
[15] Zeng, J. and T. Korsmeyer, Principles of droplet electrohydrodynamics for lab-on-a-chip. *Lab Chip*, **2004**. *4*(4): p. 265-277.
[16] Ozen, O., N. Aubry, D.T. Papageorgiou, and P.G. Petropoulos, Monodisperse drop formation in square microchannels. *Phys Rev. Lett.*, **2006**. *96*(14): p. 1-4.
[17] Tan, S.H., N.T. Nguyen, L. Yobas, and T.G. Kang, Formation and manipulation of ferrofluid droplets at a microfluidic T-junction. *J. Micromech. Microeng.*, **2010**. *20*(4).
[18] De menech, M., P. Garstecki, F. Jousse, and H.A. Stone, Transition from squeezing to dripping in a microfluidic T-shaped junction. *J. Fluid Mech.*, **2008**. *595*: p. 141-161.
[19] Van Der Graaf, S., et al., Lattice Boltzmann simulations of droplet formation in a T-shaped microchannel. *Langmuir*, **2006**. *22*(9): p. 4144-4152.
[20] Wu, L., M. Tsutahara, L.S. Kim, and M. Ha, Three-dimensional lattice Boltzmann simulations of droplet formation in a cross-junction microchannel. *Int. J. Multiphase Flow*, **2008**. *34*(9): p. 852-864.
[21] Osher, S. and J.A. Sethian, Fronts propagating with curvature-dependent speed: Algorithms based on Hamilton-Jacobi formulations. *J. Comput.l Phys.*, **1988**. *79*(1): p. 12-49.
[22] Brackbill, J.U., A continuum method for modeling surface tension. *J. Comput. Phys.*, **1992**. *100*(2): p. 335-354.
[23] Enright, D., R. Fedkiw, J. Ferziger, and I. Mitchell, A hybrid particle level set method for improved interface capturing. *J. Comput. Phys.*, **2002**. *183*(1): p. 83-116.
[24] Patankar, S., *Numerical heat transfer and fluid flow*. 1980: Hemisphere Publisher, New York.
[25] Peng, D., et al., A PDE-Based Fast Local Level Set Method. *J. Comput. Phys.*, **1999**. *155*(2): p. 410-438.
[26] Jiang, G.S. and D. Peng, Weighted ENO schemes for Hamilton-Jacobi equations. *SIAM J. Sci. Comput.*, **2000**. *21*(6): p. 2126-2143.
[27] Shu, C.W. and S. Osher, Efficient implementation of essentially non-oscillatory shock-capturing schemes. *J. Comput. Phys.*, **1988**. *77*(2): p. 439-471.
[28] Fang, C., et al., 3-D numerical simulation of contact angle hysteresis for microscale two phase flow. *Int. J. of Multiphase Flow*, **2008**. *34*(7): p. 690-705.
[29] Gaudlitz, D. and N.A. Adams, On improving mass-conservation properties of the hybrid particle-level-set method. *Computers Fluids*, **2008**. *37*(10): p. 1320-1331.